THERMAL, MAGNETIC AND STRUCTURAL ASPECTS OF TRANSITIONS IN $Mn_{0.63}Cr_{0.37}As$. THERMODYNAMIC PROPERTIES FROM 10 TO 350 K

N. KOMADA *, E.F. WESTRUM, Jr.

Department of Chemistry, University of Michigan Ann Arbor, MI 48109, USA

H. FJELLVÅG and A. KJEKSHUS

Department of Chemistry, University of Oslo, Blindern, N-0315 Oslo 3, Norway

Subambient crystallographic and magnetic structures and heat capacity on $Mn_{0.63}Cr_{0.37}As$ are measured below 350 K. A complex first order magnetic (helimagnetic H_a- to H_c-type) and structural (MnP- to MnP-type) transition, accompanied by a discontinuous unit cell volume change, and a second order magnetic [heli-(H_c) to paramagnetic] transition are observed at 165 and 219 K, respectively. The thermodynamic functions are derived and the thermodynamic characteristics of the transitions are discussed. The enthalpy and entropy of the combined MnP,H_a- to MnP,H_c- and $MnP,H_c \rightleftarrows MnP,P$-type transitions are assessed to be 124.8R K and 0.749R, respectively. Two different models for the deconvolution of the magnetic heat-capacity envelope into contributions from the MnP,H_a- to MnP,H_c- and the $MnP,H_c \rightleftarrows MnP,P$-type transitions are considered.

1. Introduction

The binary end members CrAs and MnAs of the $Mn_{1-t}Cr_tAs$ solid-solution phase have both been extensively studied due to their interesting magnetic and structural properties [1–8]. However, rather recently, more attention has been focused on $Mn_{1-t}Cr_tAs$, the complex structural and magnetic properties of which have been studied by e.g., X-ray and neutron diffraction, magnetic susceptibility, magnetization, and DSC techniques [9–13].

$Mn_{1-t}Cr_tAs$ ($\sim 0.05 < t \leqslant 1.00$) crystallizes with the orthorhombic MnP-type structure below 400 to 1200 K depending on the composition. Several structural and magnetic phase transitions occur as a function of temperature and composition. A phase diagram is presented elsewhere [13]. At 300 K paramagnetic properties are found for all compositions apart from $t \approx 0.00$. At lower temperatures, two different incommensurate mag-

netic structures are found ($\sim 0.05 < t \leqslant 1.00$). MnAs-rich samples have a so-called double a-axis spiral structure (termed H_a-type), with magnetic moments in the bc-plane, and spiral propagation direction parallel to a, while CrAs-rich samples have a double c-axis helimagnetic structure (H_c-type; magnetic moments in the ab-plane, spiral propagation along c) [3,8,10,12]. Projection of these magnetic arrangements on the ac-plane is shown in fig. 1.

In the narrow composition interval $(0.320 \pm 0.005) \leqslant t \leqslant (0.385 \pm 0.005)$ the H_c- and H_a-type magnetic structures appear as high- and low-temperature modifications (for fixed t), respectively [12,13]. Among the large category of binary and ternary MnP-type phases showing helimagnetic order [13], this is the only known example where such a transition occurs. $Mn_{0.63}Cr_{0.37}As$ undergoes the first order, hysteresis-accompanied H_a- to H_c-type transition (upon heating) at $T_{S,i} = (162 \pm 3)$ K [$T_{S,d} = (142 \pm 3)$ K], while spin disordering occurs at $T_N = (223 \pm 3)$ K [12]. $Mn_{0.63}Cr_{0.37}As$ is believed to be a good choice for a more detailed study of the low-temperature magnetic and struct-

* Present address: Mitsubishi Metal Corporation, 1-6-1 Ohte-machi, Chiyoda-ku, Tokyo 100, Japan.
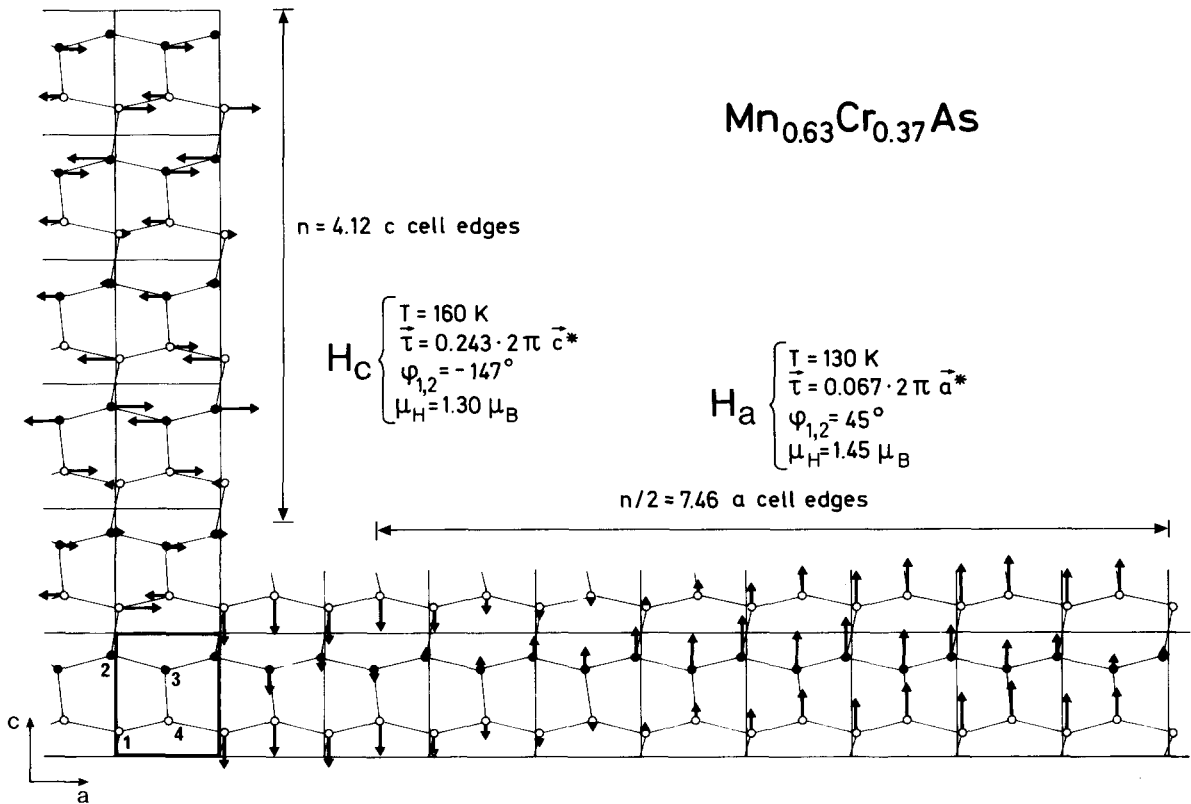
Fig. 1. Projections of the MnP,H_a- and MnP,H_c-type magnetic arrangements of $Mn_{0.63}Cr_{0.37}As$ on the *ac* plane; magnetic moments rotate in *bc*- and *ab*-plane, respectively. ○ and ● represent Mn,Cr atoms in $y = 1/4$ and $3/4$, respectively; for the numbering of these atoms see ref. [12]. Numerical magnetic structure data given on the illustration refer to 130 and 160 K for H_a- and H_c-type modes, respectively.

ural phase transitions. In this work we report on X-ray and neutron diffraction diffraction studies as well as heat-capacity measurements performed on the *same sample* of $Mn_{0.63}Cr_{0.37}As$ over the temperature range 10–350 K.

2. Experimental

Sample provenance and characterization. $Mn_{0.63}$-$Cr_{0.37}As$ was synthesized in evacuated, sealed silica tubes from MnAs and CrAs. MnAs and CrAs were made from the elements (Mn, crushed flakes, 99.99%, Johnson, Matthey & Co.; Cr, crushed flakes, 99.9999%; and As, lumps, 99.9999%, Koch-Light Laboratories) as described in ref. [12].

Six batches of $Mn_{0.63}Cr_{0.37}As$, each amounting to ~ 25 g, were synthesized. The mixtures of the binary compounds were first heated at 950°C for 7 d. The samples were carefully crushed after cooling to room temperature and subjected to two further heating cycles at 700°C for 14 d. Before the last heat treatment, the six independently synthesized batches were mixed together. After the final heat treatment the sample was slowly cooled from 700°C to room temperature at a rate of ~ 30 K h^{-1}.

The composition and homogeneity of the different samples of $Mn_{0.63}Cr_{0.37}As$ were evaluated from room temperature powder X-ray diffraction data (Guinier technique, CuKα_1 radiation, $\lambda = 154.0598$ pm, Si as an internal standard $a =$

543.1065 pm [14]. The unit cell dimensions for the present sample are in excellent agreement with values reported earlier [4].

Low temperature X-ray diffraction data were collected between 100 and 300 K with an Enraf-Nonius (FR 553) Guinier Simon camera ($CuK\alpha_1$ radiation, quartz crystal monochromatizer). The sample was kept in a rotating, sealed silica capillary, and the temperature was varied continuously at a heating or cooling rate of ~ 0.2 K min^{-1}. The temperature difference between the programmed temperature and that of the sample is estimated to be less than ± 2 K. Unit cell dimensions were obtained through least-squares refinements of the positions of 15–25 well defined Bragg reflections.

Neutron diffraction. Powder neutron diffraction data were collected with the OPUS III two-axis diffractometer accommodated at the JEEP II reactor, Kjeller. Monochromatic neutrons of wavelength 187.7 pm were obtained by reflection from (111) planes of a Ge-crystal. The scattered intensities were registered by means of a multi-counter system consisting of five ^{3}He-detectors spaced 10° apart in 2θ. Intensity data were collected in steps of 0.05° from $2\theta = 5.00$ to 85.00°. A Displex cooling unit was used to obtain temperatures between 10 and 295 K. Temperature variations were performed in steps of 5 K at heating/cooling rates of ~ 1 K min^{-1}, and the overall measuring period at each temperature was ~ 2 h. Crystal structure analyses of the thus obtained intensity data were performed according to the Hewat [15] version of the Rietveld [16] program. The scattering lengths (in fm) $b_{Mn} = -3.70$, $b_{Cr} = 3.53$ and $b_{As} = 6.4$ were adopted [17]. The magnetic structures were analysed according to the program SPIRAL [18] and the magnetic form factor for Mn^{2+} [19] was used.

Heat-capacity measurements were made in the Mark X cryostat, which is described in detail elsewhere [20], over the temperature range 10 to 350 K. A computer-operated, intermittently heated, adiabatic, equilibrium method was used. A gold-plated copper calorimeter (laboratory desig-

nation W-139) with a mass of 13.207 g, an internal volume of 22.7 cm^3, an axial entrant well for the heater/thermometer assembly, and a gold gasket for sealing, was filled in the air with 70.724 g of the gray crystalline $Mn_{0.63}Cr_{0.37}As$ powder sample. The calorimeter was evacuated to ~ 0.1 mPa immediately after weighing, and then hermetically sealed after introduction of purified helium gas (3.2 kPa at room temperature) for enhancing thermal contact to reduce equilibration times. A National Bureau of Standards calibrated, capsule-type, platinum reistance thermometer was used to determine sample temperatures according to IPTS-48 above 90.18 K and the NBS 1955 provisional scale at lower temperatures. The heat capacity of the empty calorimeter was determined in separate series of measurements, in which nearly identical amounts of Apiezon-T grease (for thermal contact between the calorimeter and the heater/thermometer assembly), helium gas, and the same gold gasket were used.

A density of 6.76 g cm^{-3} and a molar mass of 128.771 g mol^{-1} corresponding to the formula $Mn_{0.63}Cr_{0.37}As$ were used to calculate the buoyancy correction and the molar heat capacity, respectively. After adjustments for the heat capacity of the empty calorimeter, for the differences in amounts of Apiezon-T grease and helium gas between the empty and the loaded calorimeter, and for the curvature of the heat-capacity versus temperature curve, the resulting molar heat-capacity data were fitted with 13 term Tchebycheff orthogonal polynomials from 10 to 57.5 K and from 57.5 to 155 K, with six terms from 175 to 210 K, and with 10 terms from 225 to 350 K by a revised version of the FITAB [21] computer program to generate thermodynamic functions. The curvature correction was not applied to the data in the transition regions except for the data for the undercooled state. The thermodynamic functions below 10 K and in the transition regions were evaluated graphically by Simpson's rule. The heat capacity of the empty calorimeter was 16% (minimum) of the total at 10 K, 26% (maximum) at 50 K, 23% above 300 K. The standard deviations of the experimental data from the smoothed heat-capacity curve were 0.13% for the low-temperature segment (10–57.5 K), 0.06% for the next

segment (57.5–155 K), 0.05% for the third segment (175–210 K), and 0.05% for the high-temperature segment (225–350 K). Since temperature scale errors tend to cancel in the integration process, the accuracy of the thermodynamic functions is enhanced.

3. Results and discussion

Crystal and magnetic structures. The crystal structure is confirmed to be of the MnP-type (space group *Pnma*) for temperatures $10 \leqslant T \leqslant 350$ K. The Mn and Cr atoms are randomly distributed at long range over the $4c$ positions of the metal sublattice, and the average metal atom unfortunately thus obtains a low scattering length for neutrons. While the $x_{Mn,Cr}$ and z_{As} parameters are found to stay unchanged within standard deviations between 10 and 295 K, there are overall decreases in the parameters $z_{Mn,Cr}$ and x_{As} with decreasing temperature, cf. table 1. These findings are consistent with the general experimental picture for all phases which undergo the second order MnP,P $\rightleftarrows$ NiAs,P-type transition and model considerations for this transition [22–26]. The MnP, P $\rightleftarrows$ NiAs,P-type transition temperature for $Mn_{0.63}Cr_{0.37}As$ is $T_D = 690$ K [13].

The temperature variation of the unit cell di-

mensions between 10 and 300 K for the present $Mn_{0.63}Cr_{0.37}As$ sample is shown in fig. 2. The increase in b at T_N is correlated with the onset of helimagnetic order (MnP,P $\rightleftarrows$ MnP,H$_c$), while the discontinuous change in lattice constants at $T_{S,i}$ is correlated with the change in the magnetic structure (MnP,H$_a$ $\rightarrow$ MnP,H$_c$). The discontinuous unit cell compression at $T_{S,i}$ amounts to $\Delta V = V(H_c) - V(H_a) = (3.45 \pm 0.25) \times 10^6$ pm^3 or $\sim$ 2.8%.

The magnetic structures in the temperature

Table 1
Unit cell dimensions and positional parameters with standard deviations for $Mn_{0.63}Cr_{0.37}As$ as derived from Rietveld analyses of neutron diffraction data. (Nuclear R_n-factors ranging between 0.04 and 0.07, profile R_p-factors between 0.11 and 0.14.) Parameters for the magnetic structures are also included

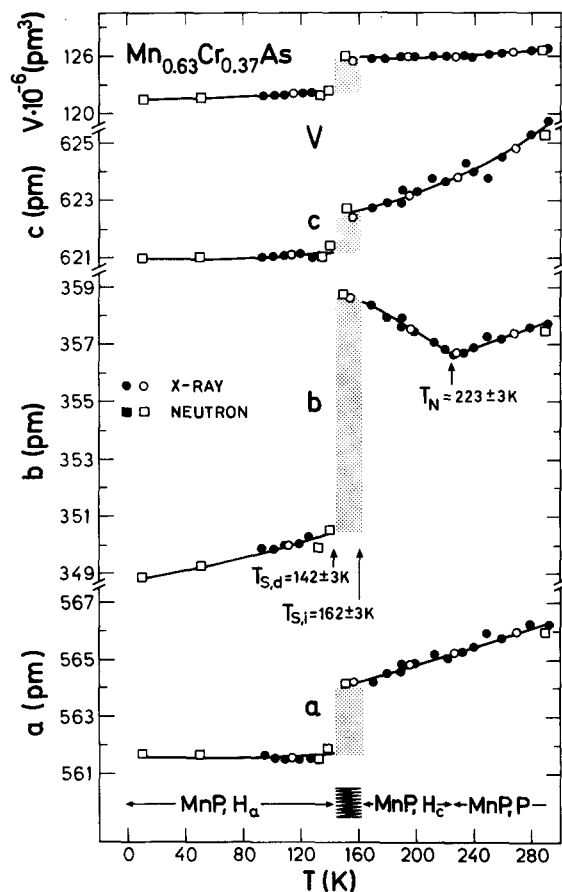| T (K)	295	160	10
Magn. state	Para	Heli–H$_c$	Heli–H$_a$
a (pm)	565.90 (5)	564.21 (4)	561.30 (5)
b (pm)	357.42 (4)	358.61 (8)	348.69 (4)
c (pm)	625.37 (9)	621.99 (15)	620.90 (5)
$x_{Mn,Cr}$	0.010 (8)	0.012 (8)	0.013 (8)
$z_{Mn,Cr}$	0.217 (8)	0.214 (8)	0.208 (8)
x_{As}	0.216 (1)	0.205 (1)	0.203 (1)
z_{As}	0.582 (2)	0.581 (2)	0.581 (2)
μ (μ_B)	–	1.30 (10)	1.84 (10)
τ	–	$0.243 \times 2\pi c^*$	$0.062 \times 2\pi a^*$
$\phi_{1,2}(°)$	–	-147 (10)	39 (10)

Fig. 2. Unit cell dimensions versus temperature for $Mn_{0.63}Cr_{0.37}As$ between 10 and 300 K. Results marked $\square$, $\blacksquare$ are obtained by neutron diffraction, $\circ$, $\bullet$ by X-ray diffraction. Open and filled symbols refer to data obtained upon cooling and heating, respectively, shading marks the hysteresis region between H$_a$- and H$_c$-type states. *Calculated* error limits do not exceed size of symbols. $T_{S,d}$ and $T_{S,i}$ determined by visual inspection of X-ray diffraction film scans.
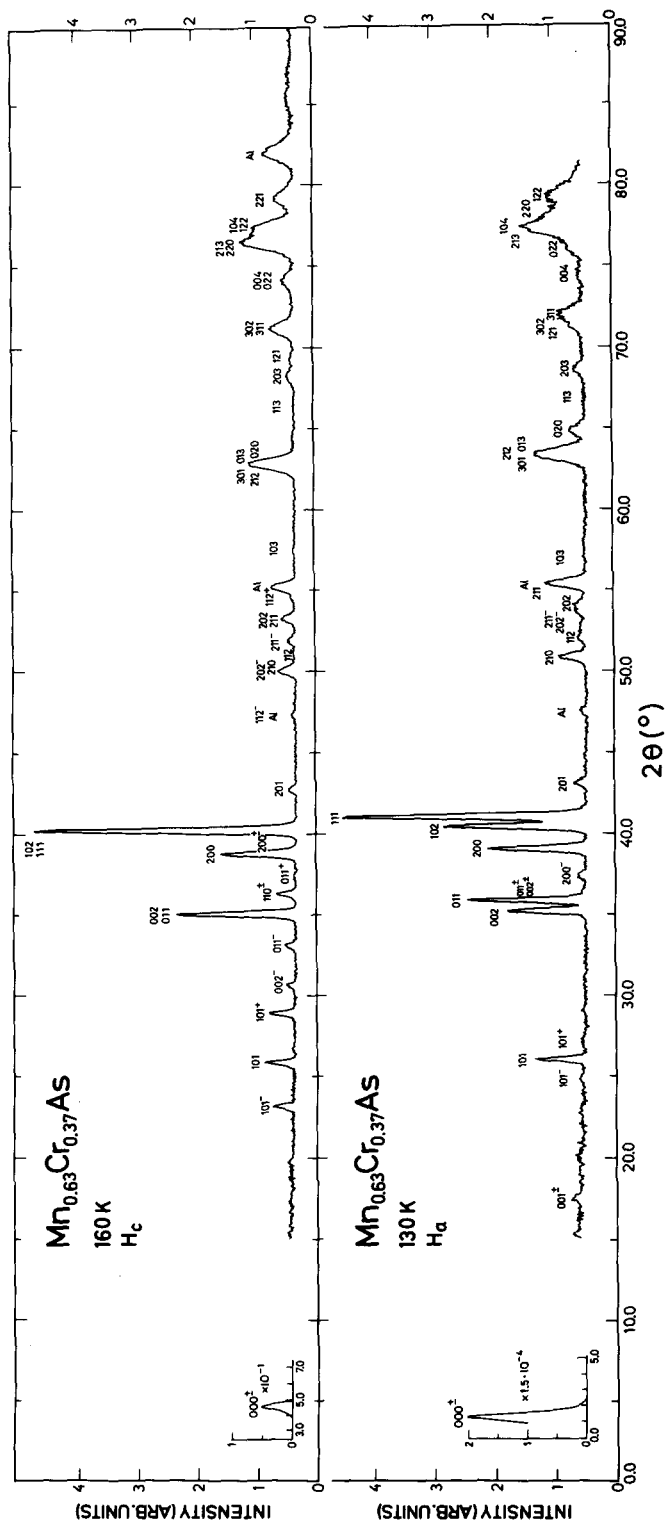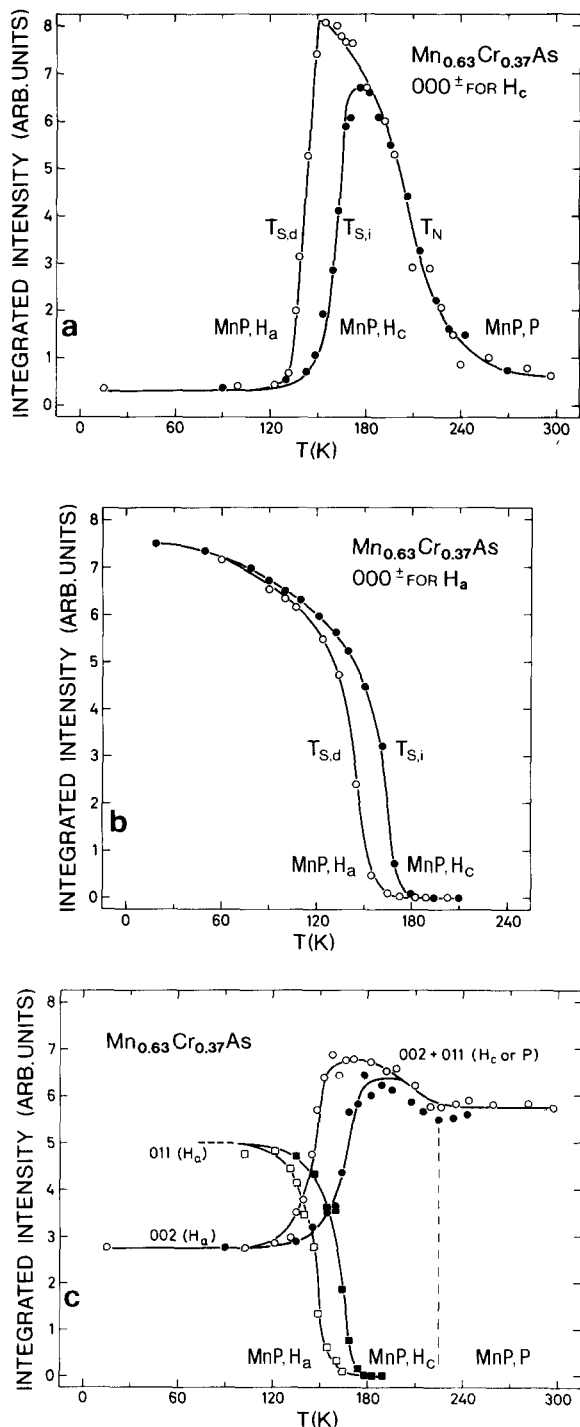
Fig. 3. Powder neutron diffraction diagrams of $Mn_{0.63}Cr_{0.37}As$ at 130 and 160 K. Indexing of the reflections is given on the illustration.

ranges $0 < T < T_{S,i}$ and $T_{S,i} < T < T_N$ are, respectively, of the H_a- and the H_c-types. The powder neutron diffraction diagrams at 130 and 160 K are shown in fig. 3, the indexing of all satellite and fundamental reflections being marked. The marked changes in both the crystallographic and magnetic components of the MnP,H_a- to MnP,H_c-type transition are clearly evident on comparing the two diffraction patterns in fig. 3. The continuous and discontinuous (viz. second and first order) character of the $MnP,H_c \rightleftarrows MnP,P$- and MnP,H_a- to MnP,H_c-type transition, respectively, is demonstrated by the integrated intensity versus temperature relationships for selected, characteristic satellite and fundamental reflections in fig. 4. The $000^{\pm}$ satellite reflections of both the H_a- and the H_c-type magnetic structures are used to determine T_S ($T_{S,i}$ or $T_{S,d}$) and T_N. The integrated intensity versus temperature relationship for these peaks gives transition temperatures in agreement with the crystal structure data presented above. The hysteresis loop of the H_a- to H_c-type transition (between heating and cooling curves, cf. fig. 4) is, in addition to the discontinuities in the unit cell dimensions, a definite proof of the first-order character of this transition. The propagation vector for the H_c-type is (0, 0, 0.243) at 160 K and (0.062, 0, 0) for the H_a-type at 10 K. The magnetic moment of the H_a-type mode decreases from $(1.84 \pm 0.10)\mu_B$ at 10 K to $(1.45 \pm 0.10)\mu_B$ at 130 K, while being $\mu_H = (1.30 \pm 0.10)\mu_B$ for the H_c-type mode at 160 K. Hence, no significant change in the size of the magnetic moment takes place at $T_{S,i}$ ($T_{S,d}$).

Fig. 1 shows a projection of the H_a- and H_c-type magnetic structures of $Mn_{0.63}Cr_{0.37}As$ on the ac-plane. The H_c-type mode has a repetition length of ~ 4.1 c-cell edges (~ 2500 pm) at 160 K while being substantially larger, ~ 14.9 a-cell edges (~ 8400 pm) for the H_a-type mode at 130 K. For the H_c-type arrangement, the spins are largely antiferromagnetically coupled, whereas they are approximately ferromagnetically coupled in the H_a-type arrangement (fig. 1).

Fig. 4. Integrated intensity of (a) $000^{\pm}$ satellite for H_c-type state, (b) $000^{\pm}$ satellite for H_a-type state and (c) 011 and 002 fundamental reflections as function of temperature. Open and filled symbols refer to data obtained upon cooling and heating, respectively.

Thermodynamic properties. The experimental molar heat capacities C_p (corrected as described in section 2) are tabulated chronologically in table 2 and presented graphically in fig. 5. The results from series II, III, and IV measurements show lower heat-capacity values for the lower-temperature MnP,H_a- to MnP,H_c-type transition than those from series V and VII. The thermal history of the sample during the calorimetric measurements (evident from table 3) shows that these data represent different degrees of completeness of conversion to the lower-temperature MnP,H_a-type phase upon cooling. However, series V and VII for which the sample was cooled to temperatures below 55 K at a slow rate of ~ 0.9 K h^{-1} in the transition region, showed the same results within the experimental error, even despite the different heating rate in the transition region during the data acquisition. Therefore, the data of these two series are considered to represent a completed phase transition, free of the complications of the undercooled state. The cooling data indicate (in concord with the X-ray and neutron diffraction data) that the conversion starts at about 150 K ($= T_{S,d}$) upon cooling irrespective of the cooling rate. Series II, III and IV data are not used to calculate smoothed heat capacity and thermodynamic functions. On the other hand, measure-

ments on the undercooled (metastable) state were intentionally performed in series VIII and IX. The sample was cooled slowly to 209 K, and then quickly from 209 K down to ~ 160 K (allowing a margin of about 10 K), and the measurement was started immediately to minimize the possibility of the onset of the phase transition. Different cooling and heating rates were employed for (the next) series IX to demonstrate reproducibility. The heat capacity in the transition region is illustrated in fig. 6. Series IX data agree with the series VIII data within $\pm 0.05\%$. No hysteresis was, however, observed for the higher-temperature $MnP,H_c \rightleftarrows MnP,P$-type transition, thus confirming the second-order nature of this transition. The smoothed heat capacity and the derived thermodynamic functions at selected temperatures are listed in table 4.

The calorimetric measurements reveal that the transition peak for the MnP,H_a- to MnP,H_c-type transition is centered at (165 ± 1) K ($= T_{S,i}$). This value agrees rather well with the X-ray [$T_{S,i} = (162 \pm 3)$ K; fig. 2] and neutron diffraction [$T_{S,i} = (162 \pm 4)$ K; figs. 4a–c] results for the same sample as well as with the DSC value ($T_{S,i} = 167$ K) reported in ref. [12]. The findings for T_N are equally satis-

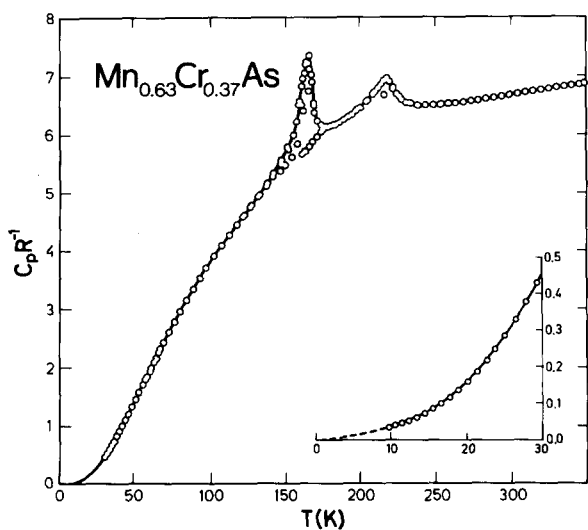Fig. 5. Experimental molar heat capacity, $C_p R^{-1}$, of $Mn_{0.63}Cr_{0.37}As$ between 10 and 350 K ($R = 8.3144$ J K^{-1}mol^{-1}).

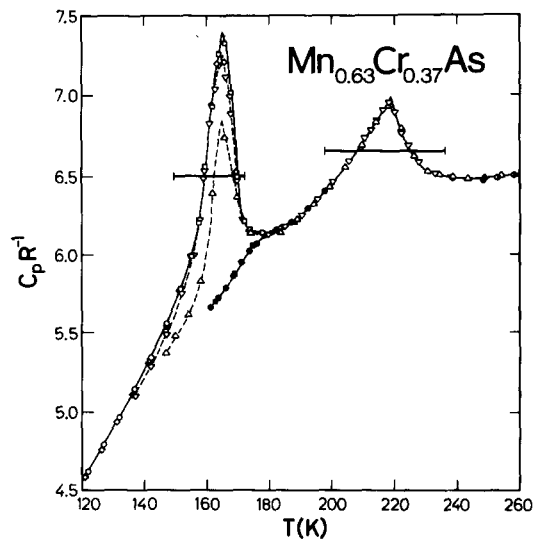Fig. 6. Experimental molar heat capacity, $C_p R^{-1}$, in the anomaly region $\oplus$: series I, $\triangle$: series II, $\triangledown$: series III, $\diamondsuit$: series IV, $\bigcirc$: series V, $\square$: series VII, $\bullet$: series VIII, $\blacksquare$: series IX.

Table 2
Experimental molar heat capacities of $Mn_{0.63}Cr_{0.37}As$ ($R = 8.3144$ J $K^{-1}mol^{-1}$)

T (K)	$C_p R^{-1}$	T (K)	$C_p R^{-1}$	T (K)	$C_p R^{-1}$	T (K)	$C_p R^{-1}$
Series I		142.11	5.288 [a,b]	189.20	6.243	38.70	0.831
		147.10	5.488 [a,b]	194.85	6.349	40.52	0.920
248.27	6.498	152.07	5.750 [a,b]	216.84	6.663 [a,c]	42.43	1.010
252.58	6.506	155.51	5.991 [a,b]	238.65	6.500	44.44	1.112
257.77	6.625	157.40	6.222 [a,b]			46.54	1.224
262.96	6.539	159.24	6.493 [a,b]	Series V		48.74	1.336
268.15	6.551	161.01	6.826 [a,b]			51.06	1.459
273.33	6.567	162.72	7.040 [a,b]	57.74	1.813	53.50	1.586
278.51	6.586	164.38	7.197 [a,b]	60.35	1.954	56.06	1.724
283.70	6.616	166.04	7.116 [a,b]	63.26	2.112	58.75	1.867
288.88	6.635	167.74	6.889 [a,b]	66.32	2.274	61.57	2.022
294.06	6.656	169.49	6.495 [a,b]	69.54	2.440	64.54	2.181
299.25	6.673	171.32	6.234 [a,b]	72.93	2.607	67.66	2.344
304.44	6.688	174.85	6.153 [a,b]	76.48	2.783		
309.62	6.713	180.02	6.142 [a,b]	80.22	2.969	Series VII	
314.79	6.739	185.14	6.183	84.15	3.161		
319.98	6.762	190.25	6.255	88.29	3.349	141.65	5.329
325.17	6.779	195.33	6.358	92.64	3.534	146.67	5.543
330.35	6.794	200.41	6.473	97.22	3.719	151.68	5.782
335.54	6.815	205.48	6.596	102.05	3.905	155.32	5.998
340.72	6.837	208.88	6.682	107.01	4.093	157.56	6.215
345.91	6.854	210.61	6.739	111.99	4.275	159.72	6.561 [a]
349.20	6.878	212.33	6.784	117.00	4.450	161.81	6.938 [a]
		214.19	6.849 [a]	122.03	4.625	163.80	7.263 [a]
Series II		216.17	6.914 [a]	127.05	4.798	165.76	7.338 [a]
		218.13	6.959 [a]	132.07	4.968	167.74	7.027 [a]
146.93	5.375 [a,b]	220.10	6.901 [a]	137.11	5.155	169.80	6.509 [a]
150.20	5.480 [a,b]	222.08	6.773 [a]	142.14	5.347	171.96	6.219 [a]
154.18	5.617 [a,b]	224.09	6.692	147.15	5.562	174.17	6.176
158.13	5.835 [a,b]	227.67	6.594	160.96	6.505 [a,c]	177.89	6.139
161.97	6.402 [a,b]	232.82	6.527				
165.79	6.744 [a,b]	237.94	6.503	Series VI		Series VIII	
169.85	6.372 [a,b]						
174.05	6.150 [a,b]	Series IV		9.75	0.035	161.27	5.666 [b]
178.73	6.134 [a,b]			10.61	0.040	163.76	5.722 [b]
183.92	6.165 [a,b]	117.27	4.456 [a,b]	11.51	0.046	166.24	5.791 [b]
189.08	6.237	121.28	4.593 [a,b]	12.42	0.053	168.72	5.872 [b]
194.22	6.332	126.33	4.765 [a,b]	13.40	0.062	171.18	5.953 [b]
199.35	6.445	131.36	4.940 [a,b]	14.46	0.073	173.63	6.026 [b]
204.47	6.564	136.39	5.117 [a,b]	15.51	0.086	176.08	6.088 [b]
209.59	6.697	141.43	5.312 [a,b]	16.57	0.100	178.53	6.133 [b]
214.14	6.838 [a]	146.46	5.526 [a,b]	17.63	0.117	182.21	6.170 [b]
218.14	6.939 [a]	151.48	5.772 [la,b]	18.78	0.137	187.24	6.219 [b]
222.20	6.800 [a]	155.12	5.994 [a,b]	20.02	0.161	192.40	6.304 [b]
226.33	6.630	157.36	6.220 [a,b]	21.26	0.188	197.53	6.412 [b]
230.44	6.543	159.51	6.545 [a,b]	22.50	0.218		
234.53	6.513	161.57	6.944 [a,b]	23.75	0.251	Series IX	
238.59	6.508	163.55	7.203 [a,b]	25.03	0.288		
243.23	6.498	165.49	7.216 [a,b]	26.39	0.330	162.93	5.703 [b]
248.43	6.504	167.46	7.009 [a,b]	27.84	0.379	168.89	5.877 [b]
253.62	6.516	169.51	6.537 [a,b]	29.30	0.431	174.88	6.060 [b]
258.81	6.527	171.66	6.233 [a,b]	30.76	0.485	180.90	6.157 [b]
		173.85	6.165 [a,b]	32.24	0.544	186.90	6.215 [b]

Table 2 (continued)

T (K)	C_pR^{-1}	T (K)	C_pR^{-1}	T (K)	C_pR^{-1}	T (K)	C_pR^{-1}
Series III		177.82	6.138	33.75	0.610		
		183.53	6.177	35.33	0.679		
				36.98	0.751		
137.11	5.109 [a,b]						

[a] Curvature correction not applied (average value).

[b] Not used in curve fit for thermodynamic functions. These points do not represent complete conversion to the lower temperature phase (see text and thermal history).

[c] Enthalpy run (large temperature increment).

factory: (219 ± 1) K, calorimetric; (223 ± 3) K, X-ray; (215 ± 5) K, neutron; and 222 K DSC.

Estimation of different contributions to the measured heat capacity. According to the conventional approach to the resolution of heat capacity, the measured C_p is a sum of an isometric lattice heat capacity, C_l, a dilation contribution which arises from the anharmonicity of the lattice vibrations, C_d, a conduction electron contribution, C_e, and a magnetic contribution, C_m, viz.

$$C_p = C_l + C_d + C_e + C_m.$$

(As a formal point it may be noted that some authors combine $C_l + C_d$ into a joint phonon contribution.) An objection to this additivity model is that it neglects (at least explicitly, vide infra) interactions between the different forms of energy storage in solids, viz. the existence of mixed heat-capacity terms of the type $C_{l,e}$, $C_{l,m}$ etc. Although more detailed models require estimates of such coupling terms, knowledge of the necessary physical parameters are not normally at hand. The present attempt to resolve the measured heat-capacity curve for $Mn_{0.63}Cr_{0.37}As$ will therefore

Table 3

Thermal history of the $Mn_{0.63}Cr_{0.37}As$ sample during the heat-capacity measurements

Cooling/Heating	Initial temperature (K)	Final temperature (K)	Cooling time (h) or Series No.	Cooling rate $(K s^{-1})$	
				at 165 K	at 215 K
Cooling	300	245	14	–	–
Heating	245	349	Series I	–	–
Cooling	349	145	35	6.3×10^{-3}	1.4×10^{-2}
Heating	145	261	Series II	–	–
Cooling	261	134	34	3.6×10^{-3}	6.7×10^{-4}
Heating	134	240	Series III	–	–
Cooling	240	115	80	4.7×10^{-4}	6.0×10^{-4}
Heating	115	241	Series IV	–	–
Cooling	241	54.2	272	2.6×10^{-4}	2×10^{-3}
Heating	54.2	172	Series V	–	–
Cooling	172	150	29	4×10^{-4}	–
Heating	150	175	–	–	–
Cooling	175	5.4	214	2.6×10^{-4}	–
Heating	5.4	69.3	Series VI	–	–
Cooling	69.3	62.9	41	–	–
Heating	62.9	181	Series VII	–	–
Cooling	310	160	55	2.4×10^{-3}	4.9×10^{-4}
Heating	160	200	Series VIII	–	–
Cooling	200	160	4	3.1×10^{-3}	–
Heating	160	190	Series IX	–	–

Table 4
Molar thermodynamic functions of $Mn_{0.63}Cr_{0.37}As$ ($R = 8.3144$ J $K^{-1}mol^{-1}$)

T (K)	C_pR^{-1}	$\dfrac{S^\circ - S^\circ(0)}{R}$	$\dfrac{H^\circ - H^\circ(0)}{R}$ (K)	$-\dfrac{G^\circ - H^\circ(0)}{RT} - \dfrac{S^\circ(0)}{R}$
0	(0)	(0)	(0)	(0)
5	(0.015)	(0.014)	(0.036)	(0.007)
10	0.037	0.030	0.159	0.014
15	0.079	0.052	0.435	0.023
20	0.161	0.085	1.016	0.034
25	0.287	0.134	2.117	0.049
30	0.457	0.200	3.959	0.068
35	0.663	0.286	6.747	0.093
40	0.893	0.389	10.63	0.124
50	1.403	0.642	22.07	0.201
60	1.935	0.945	38.75	0.299
70	2.464	1.284	60.77	0.415
80	2.956	1.645	87.89	0.546
90	3.425	2.021	119.8	0.689
100	3.828	2.403	156.2	0.841
120	4.562	3.166	240.1	1.165
140	5.265	3.920	338.1	1.505
160	6.613	4.686	453.1	1.854
Lower temperature transition				
165.0	7.408	4.903	488.3	1.943
180	6.142	5.464	584.9	2.215
200	6.460	6.124	710.3	2.573
Higher temperature transition				
219.0	6.968	6.733	837.8	2.907
220	6.916	6.765	844.8	2.925
240	6.496	7.339	976.8	3.269
260	6.529	7.860	1107	3.603
280	6.595	8.346	1238	3.924
298.15	6.671	8.763	1359	4.206
300	6.679	8.804	1371	4.235
320	6.755	9.238	1505	4.534
340	6.835	9.650	1641	4.823
350	6.872	9.848	1710	4.963

largely follow the simple additivity model, but the possible influence of significant coupling contributions is briefly discussed subsequently in this sub-section.

A newly developed theoretical model was applied to estimate the lattice contribution, C_l, since the commonly used Debye model is not accurate enough for the present purpose. The new model will be described in detail elsewhere [27], and only the parameters used for the estimation of C_l are considered here. The value 1.48 was used for the ratio of the longitudinal to transverse vibrational frequency on the basis of values for related phases. Comparison of the molar C_p-curve for $Mn_{0.63}Cr_{0.37}As$ with those for MnAs [2], CrAs [5], FeAs [28] and NiAs [28] in fig. 7 brings out similarities (which most likely reflect a resemblance in C_l) and distinctions (attributed to C_d, C_e and C_m).
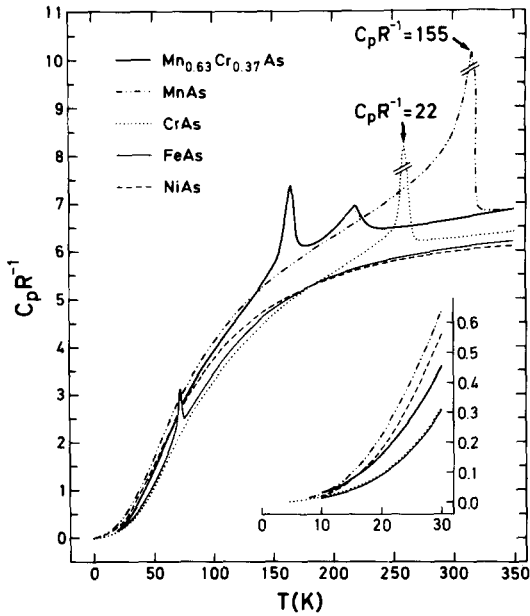
Fig. 7. C_pR^{-1} versus T for Mn$_{0.63}$Cr$_{0.37}$As in comparison with corresponding relationships for MnAs [2], CrAs [5], FeAs [28] and NiAs [28].

The value 1.48 is considered to be appropriate at the high-frequency end of the acoustical modes, although it may be too low at the low-frequency end. (The lattice-contribution model [27] postulates that the ratio, k_L/k_T, between the effective interatomic force constants for longitudinal and transverse vibrations, is constant, independent of the wave vector, whereas experimental phonon dispersions usually show that the ratio decreases with decreasing frequency.) The ratio, 2.488, of the size of the primitive cell in the spherical approximation [$2r = 2(3abc/4\pi)^{1/3} = 622.8$ pm] to the minimum interatomic distance (250.3 pm) was used to estimate the maximum frequency of the optical modes at 295 K. For the correction factor which arises from the difference in the mass of atoms in the primitive cell, the masses of As and the weighted average of Mn and Cr were used, the latter because Mn and Cr occupy a crystallographically equivalent site with random distribution. The best fit was obtained with the characteristic temperature $\theta_{TA} = 150$ K for the MnP,H$_a$-type phase. (θ_{TA} is the only

strictly *independent* variable in the lattice contribution model [27]. The definition of a particular phonon distribution function truly involves 12 parameters, but 11 of these become dependent variables through 11 relationships between crystallographic, elastic and lattice-dynamical quantities.) At the MnP,H$_a$- to MnP,H$_c$-type transition [$T_{S,i} = (162 \pm 3)$ K], however, a discontinuous increase in the unit cell volume of $\sim 2.8\%$ is observed. Therefore, a corresponding change in the vibrational frequency is expected in accordance with the characteristic temperature relation:

$$\Delta\theta_{TA}/\theta_{TA} = -\Gamma\Delta V/V,$$

where Γ is the Grüneisen constant and V the molar volume. The value of Γ for CrAs near 300 K is adopted since Mn$_{0.63}$Cr$_{0.37}$As and CrAs are isostructural with presumably similar lattice-dynamical properties. Moreover, an error in Γ would not have a significant effect on the overall heat capacity, and $\Gamma = 2$ is, in fact, frequently used in the literature without any justification. Numerically Γ is derived by application of the Grüneisen relation:

$$\Gamma = \alpha V/\kappa C_v,$$

where α is the thermal, volume expansion coefficient, κ the compressibility and C_v the isometric molar heat capacity. C_v is evaluated from C_p with:

$$C_p = C_v(1 + \alpha\Gamma T)$$

which on application of the Grüneisen relation once more gives:

$$\Gamma = \alpha V/\left(\kappa C_p - \alpha^2 VT\right).$$

A value of $\Gamma = 1.56$ is obtained on the basis of the following data for CrAs in the paramagnetic state at T = 298.15 K:

$\alpha = 1.2 \times 10^{-4}$ K^{-1} [22];

$V = 1.825 \times 10^{-5}$ m^{3}mol^{-1} [4,5,11,22,29,30];

$C_p = 52.315$ J K^{-1}mol^{-1} [5];

$\kappa = 2.83 \times 10^{-11}$ m^{2}N^{-1} [31].

The calculations give $\theta_{TA} = 143.4$ K for Mn$_{0.63}$Cr$_{0.37}$As above 165 K and for the metastable

(undercooled) MnP,H_c-type state below this temperature.

The dilation contribution, C_d, is evaluated from the expression:

$$C_d = C_1\alpha\Gamma T$$

using the following values for α derived from the diffraction data in fig. 2:

$\alpha = 4.4 \times 10^{-5}$ K^{-1}

    for the MnP,H_a-type phase;

$= -2.6 \times 10^{-5}$ K^{-1}

    for the MnP,H_c-type phase;

$= 1.1 \times 10^{-4}$ K^{-1}

    for the MnP,P-type phase below 300 K;

$= 1.2 \times 10^{-4}$ K^{-1}

    for the MnP,P-type phase above 300 K.

The thus estimated heat capacities C_1 and $C_1 + C_d$, viz. lattice C_v and C_p, respectively, are shown in fig. 8. The discontinuous changes in C_1 and $C_1 + C_d$ at $T_{S,i}$ and T_N are caused by the discontinuities in θ_{TA} and α (sign-shifts). This in turn
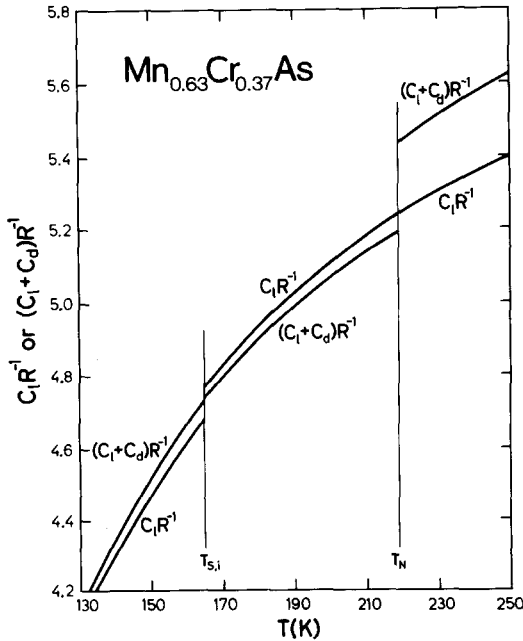
reflects the occurrence of a significant, magnetodilation coupling term, $C_{d,m}$ and probably also of additional coupling terms $C_{1,m}$ and $C_{e,m}$. Whether or not full account of these are obtained through θ_{TA}, α and the use of the simple, lattice-contribution model is not certain since direct experimental evidences are lacking and model calculations are at best difficult. If such couplings do exist, the C_m versus T relationship discussed below could give too small overall enthalpy and entropy changes for the two transitions. Having noted these uncertainties, we return to the implications of the simple additivity model.

An interesting feature of the $C_1 + C_d$ versus T relationship in fig. 8 is that the curve segments join at $T_{S,i}$ within estimated error limits. If this correspondence continues to zero kelvin, there would indeed be a very small difference in lattice entropy between the MnP,H_a- and MnP,H_c-type phases at $T_{S,i}$, which in turn implies that the major part of the transition entropy would have a magnetic and/or electronic origin despite the large volume change. Continuity in lattice heat capacity through the MnP,H_c- to MnP,P-type transition in CrAs also has been suggested by Blachnik et al. [5] despite a large volume change.

The electronic contribution, C_e, for the MnP, H_a-type phase is obtained from the C_pT^{-1} versus T^2 plot shown in fig. 9 on the assumption of a free (Fermi) carrier gas. (Note that the tempera-

Fig. 8. Model calculated lattice heat capacity, C_1R^{-1} and $(C_1 + C_d)R^{-1}$, in the anomaly region.
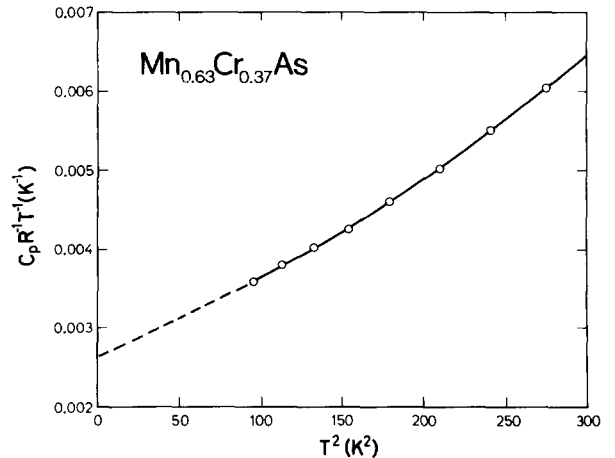

Fig. 9. $C_pR^{-1}T^{-1}$ versus T^2 for low-temperature region.

ture dependence of the low-temperature, magnetic heat capacity is yet unknown for a double helical arrangement.) The electronic contribution for the MnP,H$_c$-type phase is estimated by postulating a $V^{-2/3}$ dependence of the Fermi energy. It is moreover assumed that the effective mass and number of the carriers do not change at the MnP,H$_a$- to MnP,H$_c$-type transition, since decisive information on the electronic behaviour of the present Mn$_{0.63}$Cr$_{0.37}$As sample is lacking. (However, the latter assumption may easily be erroneous because the electronic band structure of Mn$_{1-t}$Cr$_t$As in the vicinity of $t = 0.37$ seems very sensitive to magnetic and structural changes. On the other hand, the space group remains unchanged and the unit cell dimensions a, b and c change consistently in the same direction through this transition.) The electronic contribution for the MnP,P-type phase is estimated differently. The chosen reference basis is here the asymptotically diminishing intensity of the 000$^\pm$ satellite for the H$_c$-type arrangement above $\sim$ T$_N$. In compliance with this observation, the electronic contribution for the MnP,P-type phase is adjusted so that the magnetic contribution also goes asymptotically to zero in the same temperature region. (This approach neglects the possibility that the magnetic short-range order may extend up to appreciably higher temperatures.) The resulting values for the electronic heat capacity constant, γ, are:

$\gamma = 0.0026_2 R$ K^{-1} for the MnP,H$_a$-type phase;

$\quad = 0.0026_7 R$ K^{-1} for the MnP,H$_c$-type phase;

$\quad = 0.0023_6 R$ K^{-1} for the MnP,P-type phase.

These γ values can well carry uncertainties of the order of $\pm 10\%$, but it is difficult to give more precise estimates since several quite different error-sources (viz. the uncertainty in the linear extrapolation in fig. 9, experimental errors, and approximations of the theoretical model) are involved. The discontinuous drop in the electronic heat capacity at T$_N$ does partly compensate for the abrupt increase in $C_1 + C_d$ at the same temperature.

The above γ values are higher than expected from the number of carriers estimated from the

Hall coefficient [32] and electrical resistivity [11] for Mn$_{1-t}$Cr$_t$As samples in the composition range near $t = 0.37$. However, since there are marked distinctions, as demonstrated in ref. [3], between the physical properties of samples prepared according to the same procedure as for the present Mn$_{0.63}$Cr$_{0.37}$As sample and for those made as described in refs. [11,32], no further concern is attributed to this discrepancy.

Another electronic effect which must be considered is the so-called high- to low-spin transition which has been observed for MnAs-rich solid solution phases below the NiAs,P $\rightleftarrows$ MnP,P type transition temperature T$_D$. Krokoszinski et al. [34] have proposed a model for the heat-capacity contribution originating from such a high- to low-spin transition. Magnetic susceptibility measurements [9,12,35] of Mn$_{1-t}$Cr$_t$As with $t \approx 0.37$ indeed reveal an anomalous temperature behaviour below T$_D$ which has been attributed to a gradual reduction in spin with decreasing temperature. However, no indication of an additional heat-capacity peak in the range T$_N$ < T < T$_D$ could be found in DSC scans of Mn$_{0.63}$Cr$_{0.37}$As recorded under different experimental conditions (see also refs. [12,13]). Moreover, T$_D$ = 690 K for Mn$_{0.63}$Cr$_{0.37}$As is well above the upper temperature limit (350 K) of this study. Hence, the contribution from the spin-conversion process to the present heat-capacity data is considered to be negligible.

On subtracting the thus derived, model calculated data for $C_1 + C_d$ (fig. 8) and $C_e = \gamma$T from the measured C_p curve (fig. 5) the C_m versus T relationship shown in fig. 10 is obtained. The enthalpy and entropy of the combined MnP,H$_a$- to MnP,H$_c$- and MnP,H$_c$ $\rightleftarrows$ MnP,P-type transitions, as obtained by integration according to the Simpson's rule, are:

$$\Delta_{tr}H = 124.8R \text{ K}; \quad \Delta_{tr}S = 0.749R.$$

This value for the combined transition enthalpy is about 3.5 times larger than that (36R K [12]) obtained by DSC. However, the values are incomparable since the DSC figure is based on an experimental background curve as opposed to the theoretical background defined by $C_1 + C_d + C_e$ used to derive the present value.

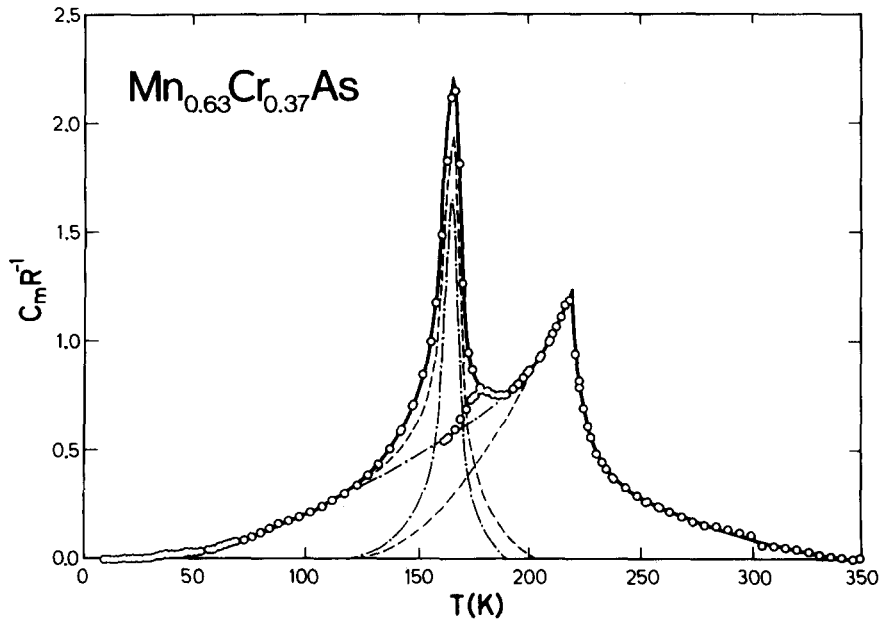The combined transition entropy is lower than

Fig. 10. Temperature variation of (molar) magnetic heat capacity, $C_m R^{-1}$. Deconvolution of the contributions from MnP,H$_a$- to MnP,H$_c$- and MnP,H$_c \rightleftarrows$ MnP,P-type transitions are illustrated by dashed and chain curves for the models I and II, respectively, discussed in the text.

the expected value ln $2.8R = 1.03R$ for ordering/disordering of 1.8 spins. However, little concern should be attached to this apparent discrepancy in view of the mentioned uncertainties in the generation of the magnetic heat capacity contribution. Lowering of γ, e.g. by 10%, enhances $\Delta_{tr}S$ by $\approx 0.1R$. The temperature variation of the accumulated magnetic entropy is illustrated in fig. 11.

Deconvolution of the magnetic heat capacity envelope. Two different approaches to the deconvolution of the magnetic heat-capacity envelope into contributions from the MnP,H$_a$- to MnP,H$_c$- and the MnP,H$_c \rightleftarrows$ MnP,P-type transitions will be considered. The first and most intuitive point of view is division of the composite C_m curve in fig. 10 in concert with the neutron diffraction results in fig. 4. That is, the MnP,H$_c$-type phase appears at ~ 130 K upon heating and the MnP,H$_a$-type phase disappears at ~ 180 K upon heating. Taking account of the slightly lower sensitivity of the neutron diffraction technique, the heat-capacity
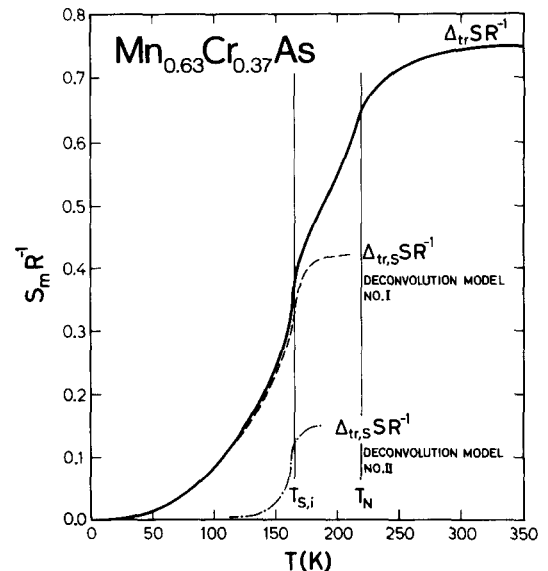

Fig. 11. Accumulated magnetic entropy versus temperature. The dashed and chain curves correspond to the deconvolution models I and II, respectively, used in fig. 10 and discussed in the text.

contribution from the $MnP,H_c \rightleftarrows MnP,P$-type transition is accordingly drawn smoothly to zero at ~ 120 K (dashed curve in fig. 10), and is then subtracted from the overall magnetic envelope. The resulting heat-capacity peak for the MnP,H_a- to MnP,H_c-type transition also obtains a reasonable morphology, as seen from the dashed curve in fig. 10. The separated enthalpy and entropy contributions for the MnP,H_a- to MnP,H_c- and $MnP,H_c \rightleftarrows MnP,P$-type transition are on this basis (designated as model I), respectively:

$$\Delta_{tr,S}H = 56.2R \text{ K}; \quad \Delta_{tr,S}S = 0.421R;$$

$$\Delta_{tr,N}H = 68.6R \text{ K}; \quad \Delta_{tr,N}S = 0.328R.$$

The large values for $\Delta_{tr,S}H$ and $\Delta_{tr,S}S$ according to this approach would require coupling between the magnetic moments and the lattice. There should, in fact, be no heat capacity contribution from a purely magnetic transition, viz. where the magnetic ordering is rearranged, but the magnitude of the magnetic moment is unchanged.

Despite apparent experimental legitimacy for such a deconvolution, one is, as a consequence of the first order character of the transition, led to regard the two transitions as inherently independent, and that either one (depending on the direction of temperature change) is essentially completed before the other starts.

The alternative approach to the deconvolution problem involves consideration of the heat-capacity peak originating from the MnP,H_a- to MnP,H_c-type transition as superimposed on that of the main peak associated with the $MnP,H_c \rightleftarrows MnP,P$-type transition. This approach has support in the experimental C_p curve for the undercooled MnP,H_c-type phase. However, it is not rooted in the diffraction data and refers to a (presently) hypothetical interpretation.

The chain curve, which separates the major and minor magnetic peaks in fig. 10, is drawn through the lowest temperature point (~ 160 K) on the C_p curve for the undercooled (metastable) MnP,H_c-type state. The arguments are the following. When the MnP,H_c-type phase is cooled rapidly (quenched) from ~ 210 to ~ 160 K the slow nucleation mechanism for the MnP,H_c- to MnP, H_a-type conversion prevents maintainance of ther-

modynamic equilibrium. Instead, small spatially dispersed centres of the MnP,H_a-type phase in a matrix of the MnP,H_c-type phase are initiated. The proposed kinetical control of the MnP,H_c- to MnP,H_a-type (and vice versa) conversion seems physically plausible in view of the dissimilarities between the magnetic arrangements (cf. fig. 1) in question. (One may also speculate as to what extent the conversion kinetics are influenced by the long- and/or short-range ordering of Cr,Mn on the metal sublattice or uncompensated stress fields [33].)

The abnormal behaviour of the heat-capacity curve for the undercooled (metastable) state between ~ 160 and ~ 190 K (fig. 10) requires an explanation. The relative excess of heat capacity in the undercooled state (compared with the chain curve) is believed to reflect a certain (slow with time and slight in proportion) growths of the H_a-type domains. When the undercooled state is heated above 180 K the MnP,H_a- to MnP,H_c-type conversion proceeds in the normal manner and the two heat-capacity curves merge. On this basis it is proposed that ~ 190 to ~ 180 K is the critical temperature region where $Mn_{0.63}Cr_{0.37}As$ has to be cooled rapidly in order to obtain the undercooled MnP,H_c-type state.

The resolved enthalpy and entropy contributions for the MnP,H_a- to MnP,H_c- and $MnP,H_c \rightleftarrows MnP,P$-type transitions according to the second deconvolution process (designated as model II), are respectively:

$$\Delta_{tr,S}H = 25.1R \text{ K}; \quad \Delta_{tr,S}S = 0.15R;$$

$$\Delta_{tr,N}H = 99.7R \text{ K}; \quad \Delta_{tr,N}S = 0.60R.$$

A physically attractive feature of this set of transition enthalpies and entropies is that $\Delta_{tr,S}H$ and $\Delta_{tr,S}S$ are considerably smaller than those accorded by the first deconvolution process. (The distribution of the accumulated magnetic entropy between the transitions according to the two deconvolution models is illustrated in fig. 11.) Nevertheless, the coupling between the magnetic moments and the lattice must still be appreciable. To further resolve this problem we propose to examine $Mn_{0.70}Cr_{0.30}As$ and $Mn_{0.60}Cr_{0.40}As$ (subject to either the MnP,H_a- to MnP,P- or the $MnP,H_c \rightleftarrows MnP,P$-type

transition, respectively [12]) as continuation of this study.

References

[1] N. Menyuk, J.A. Kafalas, K. Dwights and J.B. Goodenough, Phys. Rev. 177 (1969) 942.
[2] F. Grønvold, S. Snildal and E.F. Westrum, Jr., Acta Chem. Scand. 24 (1970) 285.
[3] K. Selte, A. Kjekshus, W.E. Jamison, A.F. Andresen and J.E. Engebretsen, Acta Chem. Scand. 25 (1971) 1703.
[4] H. Boller and A. Kallel, Solid State Commun. 9 (1971) 1699.
[5] R. Blachnik, G. Kudermann, F. Grønvold, A. Alles, B. Falk and E.F. Westrum, Jr., J. Chem. Thermodyn. 10 (1978) 507.
[6] A. Zięba, K. Selte, A Kjekshus and A.F. Andresen, Acta Chem. Scand. A32 (1978) 173.
[7] S.L. Pinjare and K.V.S. Rama Rao, J. Magn. Magn. Mat. 30 (1982) 27.
[8] A.F. Andresen, H. Fjellvåg and B. Lebech, J. Magn. Magn. Mat. 43 (1984) 158.
[9] N. Kazama and H. Watanabe, J. Phys. Soc. Japan 30 (1971) 1319.
[10] K. Selte, A. Kjekshus, P.G. Peterzéns and A.F. Andresen, Acta Chem. Scand. A32 (1978) 653.
[11] R. Wöhl, H. Berg and K. Bärner, Phys. Stat. Sol. (a) 57 (1980) 179.
[12] H. Fjellvåg and A. Kjekshus, Acta Chem. Scand. A38 (1984) 1.
[13] H. Fjellvåg and A. Kjekshus, Acta Chem. Scand. A39 (1985) 671.
[14] R.D. Deslatters and A. Henins, Phys. Rev. Lett. 31 (1973) 972.
[15] A.W. Hewat, The Rietveld Computer Program for the Profile Refinement of Neutron Diffraction Powder Patterns Modified for Anisotropic Thermal Vibrations, UKAERE Harwell Report RRL 73/897 (1973).
[16] H.M. Rietveld, J. Appl. Crystallogr. 2 (1969) 65.
[17] J.E. Engebretsen, Computer Programmes for Elastic Scattering of Neutrons from Crystalline Powders, IFA, Kjeller (1970).

[18] L. Koester and W.B. Yelon, in: Neutron Diffraction Newsletter, ed. W.B. Yelon, Missouri (1983).
[19] R.E. Watson and A.J. Freeman, Acta Crystallogr. 14 (1961) 27.
[20] E.F. Westrum, Jr., Computerized Adiabatic Thermophysical Calorimetry, in: Proceedings NATO Advanced Study Institute on Thermochemistry at Viana do Castello, Portugal, ed. M.A.V. Ribeiro de Silva (Reidel, New York, 1984) p. 745.
[21] B.H. Justice, The FITAB Program (Thermal Data Fitting with Orthogonal Functions and Combined Table Generation), COO-1149-143 NTIS, Washington DC (1969).
[22] K. Selte and A. Kjekshus, Acta Chem. Scand. 27 (1973) 3195.
[23] K. Selte, A. Kjekshus and A.F. Andresen, Acta Chem. Scand. 27 (1973) 3607.
[24] H.F. Franzen, C. Haas and F. Jellinek, Phys. Rev. B10 (1974) 1248.
[25] H. Fjellvåg and A. Kjekshus, J. Solid State Chem. 59 (1985) 9.
[26] H. Fjellvåg, A. Kjekshus and S. Stølen, J. Solid State Chem. 64 (1986) 123.
[27] N. Komada and E.F. Westrum, Jr., to be published.
[28] F. Grønvold and E.F. Westrum, Jr., to be published.
[29] Crystal Data. Determinative Tables, Vol. II. Inorganic Compounds, 3rd. ed., J.D.H. Donnay and H.M. Ondik (gen. eds.), US Dept. of Commerce, NBS, The Joint Committee on Powder Diffraction Standards (1973).
[30] K. Selte, H. Fjellvåg, A. Kjekshus and A.F. Andresen, Acta Chem. Scand. A33 (1979) 727.
[31] V.I. Kamenev and E.A. Zavadskii, Fiz. Tverd. Tela (Leningrad) 20 (1978) 933. (Sov. Phys. Solid State 20 (1978) 541.)
[32] H.J. Krokoszinski and K. Bärner, J. Magn. Magn. Mat. 21 (1980) 221.
[33] A.F. Andresen, K. Bärner, H. Fjellvåg, K. Heinemann, A. Kjekshus and U. Sondermann, J. Magn. Magn. Mat. 58 (1986) 287.
[34] H.J. Krokoszinski, C. Santandrea, E. Gmelin and K. Bärner, Phys. Stat. Sol. (b) 113 (1982) 185.
[35] R. Wöhl and K. Bärner, J. Magn. Magn. Mat. 21 (1980) 80.